PHYSICAL REVIEW B **99**, 155425 (2019)

Angular-momentum selectivity and asymmetry in highly confined wave propagation along sheath-helical metasurface tubes

Yarden Mazor[1,*] and Andrea Alù[1,2,3,4,†]
[1]Department of Electrical and Computer Engineering, The University of Texas at Austin, Austin, Texas 78712, USA
[2]Photonics Initiative, Advanced Science Research Center, City University of New York, New York, New York 10031, USA
[3]Physics Program, Graduate Center, City University of New York, New York, New York 10026, USA
[4]Department of Electrical Engineering, City College of New York, New York, New York 10031, USA

(Received 26 November 2018; revised manuscript received 5 April 2019; published 25 April 2019)

Highly confined surface waves present unique opportunities to enhance light interactions with localized emitters or molecules. Hyperbolic dispersion in metasurfaces allows us to tailor and manipulate surface waves, enhancing the local density of states over broad bandwidths. So far, propagation on this platform was mainly studied in planar geometries, which facilitates the analysis but somehow limits the realm of possibilities. Here we show that "wrapping" hyperbolic metasurfaces into tubes may greatly enrich the wave propagation dynamics along their axis. This system shows strong interaction with fields and sources carrying optical angular momentum and pronounced field asymmetries, and opens pathways to valley-specific excitation and routing. In addition, we demonstrate that various parameter regimes enable strong spin/helicity momentum locking.

DOI: 10.1103/PhysRevB.99.155425

I. INTRODUCTION

Propagation of surface waves along planar structures has been a vastly studied subject over time. In the past decade, this subject has seen increased interest in the context of plasmonics and the emergence of metasurfaces [1]—thin sheets of matter with a carefully engineered response to electromagnetic fields offering new opportunities to control and manipulate the fields. Among the numerous applications metasurfaces may have, more relevant to the present work is the research unveiling phenomena in surface wave propagation. To model the metasurface response, the surface impedance concept is used in many cases [2]. Propagation of surface waves on impedance metasurfaces has been extensively studied [3–5], presenting the flexibility offered by tailoring the surface impedance components to control and steer the surface wave fields. By considering additional degrees of freedom to the metasurface response, such as anisotropy and bianisotropy (magnetoelectric coupling) [6] we can further tailor the overall reflection/transmission [7,8] and propagation characteristics [4,9]. These additional parameters can lead to exotic responses, such as hyperbolic metasurfaces [10–14], that may support propagation of surface waves with a hyperbolic dispersion, allowing highly confined guiding and Purcell enhancement over broad bandwidths. Combined with modern nanofabrication techniques, graphene flexibility and tunability opens a realistic route towards implementing these phenomena in practical devices [11].

Surface waves guided along cylindrical boundaries have also been researched, following the pioneering work of Sommerfeld [15] that introduced wave propagation along the boundary of a metallic cylinder with finite conductivity. This study was extended in [16], both elaborating on the case of a smooth boundary, and discussing a corrugated one. In [17] the plasma response of the metal was also considered as a model of the material response. Azimuthal leaky surface waves, which propagate in the $\hat{\varphi}$ cylindrical direction rather than in the axial one, were also studied in [18,19] quantifying their radiation properties.

While several earlier works have discussed propagating waves of the form $e^{-jn\varphi}e^{-jk_z z}$ [20], the concept of orbital angular momentum of light was introduced in [21]. Since then, many applications for such waves were found, thoroughly reviewed, and presented in [22]. In the context of surface waves, and serving as an inspiration from which our work draws some of its roots, Refs. [23,24] present perfectly conducting sheath helices—cylinders allowing current only at a specific angle with respect to the cylinder axis. These structures support axial propagation of higher order, highly confined circular modes carrying optical angular momentum (OAM), where a mode with specific n has asymmetric guiding properties.

Upon the emergence of carbon nanotubes, a model of a cylindrical impedance surface was employed for several configurations [25,26] to study their electrodynamics and wave guiding properties, a model which we later use here. Cylindrical and spherical sheath metasurfaces have also been considered as candidates for cloaking [27–29] and engineering nanoparticle resonant response [30]. Cylindrical surface wave propagation was also considered in [31] for a dispersive plasma cylinder model, were it was shown that all modes converge towards specific frequencies associated with the plasma and magnetic resonance frequencies. Scattering from such cylinders was also studied in [31,32]. With recent advances in manufacturing techniques, we envision more complex cylindrical surfaces made of carefully designed and arranged inclusions. In the context of scattering, Ref. [33]

---

[*] yardenm@utexas.edu
[†] aalu@gc.cuny.edu

2469-9950/2019/99(15)/155425(7)

lays the foundations for the analysis of scattering from this type of cylindrical bianisotropic metasurface, where a method to extract the required metasurface design for a prescribed response is discussed. In [34], a structure made of a hyperbolic metamaterial deposited on a glass tube is studied for directional emission and Purcell enhancement (with extraordinary hyperbolic material axis perpendicular to the cylinder axis). The directionality and enhancement (in terms of cylindrical azimuthal scattering angle φ) arises from the metamaterial properties in addition to an asymmetric depositing process resulting in an azimuthal gradient of the deposition thickness.

In this work, we study a cylindrical surface made of a planar hyperbolic metasurface (used here and throughout the paper to indicate a surface with opposite signs of surface admittance coefficients) rolled into a tube in various configurations, yielding a cylindrical sheath with opposite current responses in two perpendicular directions. The modes propagating along the cylinder axis present extreme dispersion asymmetry. We show that by incorporating a magnetic surface response, the asymmetries can be enhanced, and asymmetric field distributions localized inside and outside the cylinder can be obtained. We examine propagating waves in the context of the electromagnetic helicity [35,36], and explore different helicity regimes for different surface parameters. These cylindrical metasurfaces reveal opportunities for highly asymmetric interaction with OAM/spin carrying waves such as unidirectional excitation of modes.

II. GEOMETRY AND FORMULATION OF THE PROBLEM

The geometry under consideration is shown in Fig. 1. To construct the studied cylindrical sheath, it is intuitive to think of a thin, planar surface folded (or rolled) along the direction of a specific guide line [dashed line in both Figs. 1(a) and 1(b)]. The principal axes of the planar surface are z', y' shown in Fig. 1(a) (with blue and red lines parallel to them, respectively), whereas the cylinder axis z makes an angle θ with z'. The response of the cylindrical sheath to applied electromagnetic fields can be described using the boundary conditions [37]

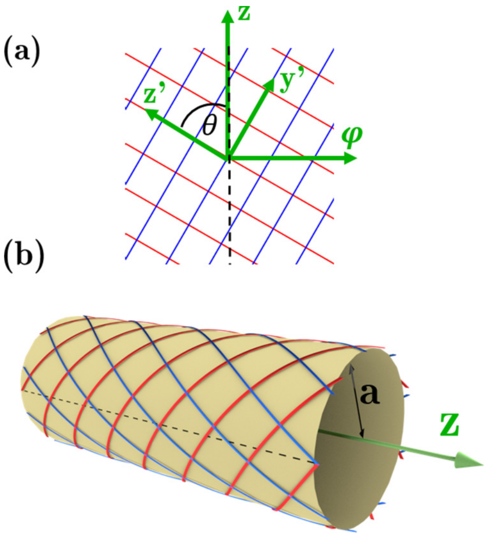

FIG. 1. The geometry under analysis. (a) The principal axes z', y' over which the constitutive relations tensors in the reference planar surface are given. The z axis indicates the direction of the cylinder axis, and the φ axis is the azimuthal direction after the folding. (b) When rotated and folded they form a skewed reference system over the surface of the cylinder with angle θ.

$$\begin{aligned}\hat{\mathbf{r}} &\times (\mathbf{H}^o - \mathbf{H}^i)_{r=a}\\ &= \mathbf{J}_s = \tfrac{1}{2}\underline{\underline{\mathbf{Y}}}_s\left(\mathbf{E}^i_{\tan} + \mathbf{E}^o_{\tan}\right) + \tfrac{1}{2}\underline{\underline{\mathbf{a}}}\left(\mathbf{H}^i_{\tan} + \mathbf{H}^o_{\tan}\right), \end{aligned} \tag{1}$$

$$\begin{aligned}-\hat{\mathbf{r}} &\times (\mathbf{E}^o - \mathbf{E}^i)\\ &= \mathbf{J}_{ms} = \tfrac{1}{2}\underline{\underline{\mathbf{Z}}}_{ms}\left(\mathbf{H}^i_{\tan} + \mathbf{H}^o_{\tan}\right) + \tfrac{1}{2}\underline{\underline{\mathbf{b}}}\left(\mathbf{E}^i_{\tan} + \mathbf{E}^o_{\tan}\right), \end{aligned} \tag{2}$$

where the superscripts o (i) refer to fields outside (inside) the cylinder. Here, $\mathbf{J}_s$, $\mathbf{J}_{ms}$ are the tangential electric and magnetic currents on the surface of the cylinder, $\underline{\underline{\mathbf{Y}}}_s$ is the electric surface admittance, $\underline{\underline{\mathbf{Z}}}_{ms}$ is the magnetic surface impedance, and $\underline{\underline{\mathbf{a}}}$, $\underline{\underline{\mathbf{b}}}$ are the bianisotropic electric-magnetic coupling tensors. The suffix *tan* denotes field components tangent to the cylinder surface ($\hat{\varphi}$, $\hat{\mathbf{z}}$). Assuming lossless, reciprocal, and local surfaces renders $\underline{\underline{\mathbf{Y}}}_s$, $\underline{\underline{\mathbf{Z}}}_{ms}$ purely imaginary and symmetric and $\underline{\underline{\mathbf{a}}}$, $\underline{\underline{\mathbf{b}}}$ are real and satisfy $\underline{\underline{\mathbf{b}}} = -\underline{\underline{\mathbf{a}}}^T$ [37,38]. The rotation relation between the response matrices of the planar surface in his principal axes z', y' [defined as $\underline{\underline{\mathbf{Y}}}^p_s$, $\underline{\underline{\mathbf{Z}}}^p_{ms}$, $\underline{\underline{\mathbf{a}}}^p$, $\underline{\underline{\mathbf{b}}}^p$ throughout the paper, corresponding to the surface in Fig. 1(a)], and the matrices of the cylindrical structure $\underline{\underline{\mathbf{Y}}}_s$, $\underline{\underline{\mathbf{Z}}}_{ms}$, $\underline{\underline{\mathbf{a}}}$, $\underline{\underline{\mathbf{b}}}$ is detailed in Appendix A. In the following, we assume the surrounding medium to be vacuum.

In cylindrical coordinates, the $\hat{\mathbf{z}}$ components of the surface wave electromagnetic (EM) fields guided along the cylinder can be written as [39]

$$\begin{aligned} E_z &= \begin{Bmatrix} A^i_n I_n(\tau r) \\ A^o_n K_n(\tau r) \end{Bmatrix} e^{-jk_z z} e^{-jn\varphi}, \\ H_z &= \begin{Bmatrix} B^i_n I_n(\tau r) \\ B^o_n K_n(\tau r) \end{Bmatrix} e^{-jk_z z} e^{-jn\varphi}, \end{aligned} \tag{3}$$

where A^i_n and B^i_n are the amplitudes of transverse-magnetic (TM) and transverse-electric (TE) wave inside the cylinder, and A^o_n, B^o_n outside the cylinder (this notation is used throughout the paper) where $e^{j\omega t}$ time convention is used. I_n and K_n are the modified Bessel functions of the first and second kind. For surface waves to be guided, there needs to be a real k_z solution satisfying $k_z^2 = k_0^2 + \tau^2 > k_0^2$, with $k_0 = \omega\sqrt{\varepsilon_0\mu_0} = \omega/c$ the free-space wave number. In the dispersion curve, such a mode would appear below the light lines which correspond to propagation with wave number k_0. The other field components are calculated from Eq. (3) using Maxwell's equations (see Appendix A) and the properties of the impedance surface are taken into account through the boundary conditions in Eqs. (1) and (2). It should also be stressed that due to the complex surface responses that we study, in general the propagating waves do not possess a "pure" TE/TM nature, but rather a mixed state between the two.

III. ASYMMETRIC PROPAGATION OVER FOLDED ELECTRIC METASURFACES

We start our analysis by considering a planar surface with only a nonzero electric surface admittance tensor of the form

$$\underline{\underline{\mathbf{Y}}}_s^p = \begin{pmatrix} Y_{y'y'} & 0 \\ 0 & Y_{z'z'} \end{pmatrix} = \frac{j}{\eta_0}\begin{pmatrix} X_{y'y'} & 0 \\ 0 & X_{z'z'} \end{pmatrix}, \tag{4}$$

We then apply the rotation operators, and obtain the surface admittance tensor in the $\varphi - z$ coordinate system corresponding to the cylindrical geometry

$$\underline{\underline{\mathbf{Y}}}_s = \begin{pmatrix} Y_{\varphi\varphi} & Y_{\varphi z} \\ Y_{z\varphi} & Y_{zz} \end{pmatrix} = \frac{j}{\eta_0}\begin{pmatrix} X_{y'y'}\cos^2\theta + X_{z'z'}\sin^2\theta & (X_{y'y'} - X_{z'z'})\sin\theta\cos\theta \\ (X_{y'y'} - X_{z'z'})\sin\theta\cos\theta & X_{y'y'}\sin^2\theta + X_{z'z'}\cos^2\theta \end{pmatrix}. \tag{5}$$

A. Single-direction currents

As a preliminary case, let us first gradually extend the work in [23,24], examining the special case of $X_{y'y'} = 0$. The dispersion equation becomes

$$\frac{I_n{}'(\tau a)K_n{}'(\tau a)}{I_n(\tau a)K_n(\tau a)} = -\frac{(-nk_z a + a^2\tau^2\cot\theta)^2}{k_0^2 a^4\tau^2} - \frac{1+\cot^2\theta}{k_0 a X_{z'z'} I_n(\tau a)K_n(\tau a)}, \tag{6}$$

tending to the relation presented in [23,24] when $X_{z'z'} \to \pm\infty$. $I_n{}', K_n{}'$ are the first derivatives of the modified Bessel functions with respect to the argument. A dispersion plot is shown in Figs. 2(a) for $\theta = \pi/4, X_{z'z'} = -4$ and since we have chosen an inductive surface with $X_{z'z'} < 0$, the EM fields are quasi-TM in nature.

We see an interesting asymmetry in the band diagram associated with the OAM direction of the mode, where a specific mode n has different propagation features to opposite propagation directions. This asymmetry comes from the fact that the sheath helix has a specific "handedness." When a mode n propagates in opposite directions, the rotation direction of the phase flips as opposed to the handedness of the sheath helix which stays the same, making the waves and the helix interact differently. As expected based on time-reversal symmetry considerations, the $-n$ mode will have the opposite relations. It is instructive to examine the dispersion relation (6) in the low-frequency limit satisfying $k_z \gg k_0$, in a similar manner to [24] (see additional remarks in Appendix B). This yields

$$k_0 a = -\frac{X_{z'z'}}{4|n|}\sin(2\theta)(-n + k_z a\cot\theta)^2. \tag{7}$$

For inductive surfaces, satisfying $X_{z'z'} < 0$, each higher-order mode has the tangency point of its dispersion with the $k_z a$ axis shifted horizontally by approximately $\Delta k_z a = \tan\theta$. The approximate parabolic shape of the dispersion also indicates low-frequency symmetry around $k_z a = n/\cot\theta$, rendering this constant as a basic characteristic of the guiding structure.

This case is a platform for interesting directional effects when such a waveguide interacts with a wave carrying angular momentum due to the asymmetry present.

B. Folded hyperbolic metasurface

Surface wave propagation on hyperbolic metasurfaces have been shown to support many interesting phenomena, including broadband, highly confined surface waves, and enhanced local density of states. In the following, we show that the application of these properties in cylindrical tubes combines and couples them with orbital angular momentum, which can lead to sorting and routing of valley selective excitations [40]. The asymmetry outlined in the previous section can be pushed further if we examine a folded hyperbolic metasurface in the same configuration, considering $X_{y'y'} > 0$ (or in general the opposite sign of $X_{z'z'}$), in Eqs. (4) and (5). For simplicity, we will focus on the special case $|X_{y'y'}| = |X_{z'z'}| = X$ with $\theta = 45°$. The dispersion equation in this scenario becomes

$$k_0 a(1 - X^2\tau^2 a^2 I_n K_n I_n{}' K_n{}') - 2nXk_z a I_n K_n = 0, \tag{8}$$

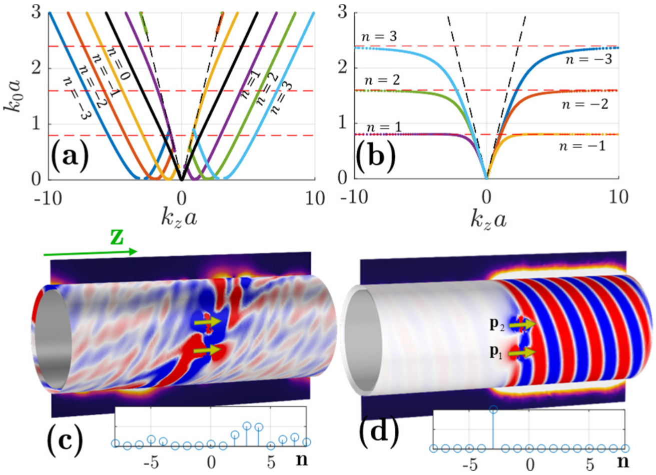

FIG. 2. (a) Surface wave dispersion curves for the folded cylindrical surface when only $X_{z'z'} \neq 0$ in Eq. (4) with $X_{z'z'} = -4$ and $\theta = \pi/4$ allowing current to flow only in a direction making 45° with the cylinder axis. Dashed black lines show the light lines, $k_0 = \omega/c$. (b) Surface wave dispersion curves for a folded hyperbolic metasurface with $X_{y'y'} = 4, X_{z'z'} = -4$ and $\theta = \pi/4$. Dashed black lines shown the light lines. The mode $n = 0$ is not present, as it does not propagate. (c) E_z sampled close to cylinder surface ($r = 1.02a$), when exciting with two dephased electric dipoles. The cylinder properties correspond to the dispersion in panel (a). The black, perpendicular panels show the electric-field intensity, where we see the fast decay as the distance from the cylinder increases. The inset shows the modal content of the fields near the cylinder, showing a mixture of many modes. (d) Same as (c), but corresponding to the cylinder properties matching the dispersion in panel (b). Highly directional excitation is observed, and pronounced mode selectivity with a single mode propagating ($n = -3$).

and the corresponding dispersion curves are shown in Fig. 2(b) for $X_{z'z'} = -X = -4$. The asymmetry with respect to the mode index is more extreme here, and positive angular-momentum modes can propagate only to the left, whereas negative angular-momentum propagates to the right. This OAM-momentum coupling is reminiscent of the edge state spin-momentum coupling in photonic topological insulators [41] and in the vicinity of hyperbolic metamaterial slabs [42]. For $n = 0$ Eq. (8) has no real solutions for τ, therefore the zero-index mode is not supported at all. Following this, if we try to excite this waveguide with OAM neutral excitation (any field/source pattern that would be invariant as a function of φ in cylindrical coordinates), no propagation of waves will occur since the projection of such an excitation on the propagating modes will be zero [43]. Each mode has a horizontal asymptote [red dashed lines in Fig. 2(b)] in frequencies $f_{r,n}$ that satisfy (calculation remarks in Appendix B)

$$\frac{2\pi f_{r,n} a}{c} = \frac{4|nX|}{4 + X^2}, \tag{9}$$

corresponding to surface waves highly confined to the tube. In this scenario, the modes have balanced TM and TE nature (fields of both polarizations are excited in comparable intensities), implying that they can strongly interact with a wide range of polarizations, with an ideal optical response to sort angular momentum and valley responses. Operating close to $f_{r,n}$, we expect highly mode-selective operation, due to the significant differences in mode confinement, and cutoff of the lower modes.

To examine these opportunities, we consider two nearby localized emitters with same magnitude polarized along $\hat{\mathbf{z}}$, but with different phase, represented by yellow vectors in Figs. 2(c) and 2(d) located at $r = 1.02a$. Such a source is used as a simple version of an excitation that couples efficiently to a specific value of orbital angular momentum n. Naturally, a mode n would best couple to a current source of the form $J_z = J_{z0} e^{-jn\varphi}$, and our two-dipole source is a two-point sampling of this optimal current distribution. The phase difference is chosen to couple to the $n = -3$ mode, and the excitation frequency is $0.985 f_{r,3}$. We have used COMSOL electromagnetic solver [44] to simulate the response of the studied structure to this excitation, where the emitters were modeled as electric point dipoles $\mathbf{p} = p\hat{\mathbf{z}}$.

When the emitters excite the helical tube corresponding to the dispersion in Fig. 2(a), we see in Fig. 2(c) that many modes are excited as we cannot see a distinct a wave pattern corresponding to a specific n. Close to the face of the cylinder we plot E_z, and on the planar panels perpendicular to the cylinder we plot the electric field intensity. The insets show the relative intensity of each mode n [45], and no directionality is noticed. Figure 2(d) shows the same excitation when applied to the folded hyperbolic metasurface, displaying highly mode-selective propagation and directionality. This can allow us to design emitters that strongly couple and launch specific angular momentum values using finite tube sections. Additional insights can be gained by examining the optical helicity density $\mathfrak{S}$ [35,46] for the modes supported by the folded hyperbolic metasurface, as calculated in Appendix B. Since our interest is focused on the highly confined modes, this calculation can be greatly simplified by examining $\mathfrak{S}_\infty = \mathfrak{S}(k_z \gg k_0)$. In particular, it follows that $\mathrm{sgn}(\mathfrak{S}_\infty^{i,o}) = \pm \mathrm{sgn}(X)$.

This can help customize the way our waveguide interacts with spin and helicity carrying sources, such as in the case of valley excitons. In particular, we envision directional sorting and routing of valley excitons [40] coupled to these cylinders, using the aforementioned interactions when folded hyperbolic metasurfaces are coated with excitonic layers around the resonant frequencies of the various modes.

IV. ASYMMETRY ENHANCEMENT USING A SURFACE MAGNETIC IMPEDANCE

By virtue of duality, folded hyperbolic metasurfaces characterized by only magnetic impedance in (4) will present dual propagation features to the case analyzed in Fig. 2. Interesting opportunities arise if we combine these two responses, further enhancing the asymmetry and directionality of the supported modes. As a testbed, we first examine the case of a *planar* surface with the same electric response shown in Eq. (4), supplemented by

$$\underline{\underline{\mathbf{Z}}}^p_{ms} = \eta_0^2 \underline{\underline{\mathbf{Y}}}^p_s, \quad \mathbf{a}^p = \mathbf{b}^p = \begin{pmatrix} 0 & \Omega \\ -\Omega & 0 \end{pmatrix}. \tag{10}$$

If $X_{y'y'}$, $X_{z'z'}$ are with opposite signs, and we combine it with a properly tailored value of Ω, the modal asymmetry manifests through an interestingly one-sided field distribution of the propagating fields, as shown in Fig. 3(a). The Ω response is required to tailor the cross interaction between the electric and magnetic fields, which gives rise to this field asymmetry, as balanced electric and magnetic currents can excite highly asymmetric field distribution [47].

Bearing this example in mind, we notice (Appendix A) that high-order guided cylindrical modes contain an inherent and rich coupling between electric and magnetic fields, allowing us to achieve similar asymmetries in the cylindrical case, without the need for an Ω-type response. All the cases we examine are based on an electric-magnetic surface described [similarly to Eq. (4)] by

$$\underline{\underline{\mathbf{Y}}}^p_s = \frac{j}{\eta_0}\begin{pmatrix} X & 0 \\ 0 & -X \end{pmatrix}, \quad \underline{\underline{\mathbf{Z}}}^p_{ms} = j\eta_0 \begin{pmatrix} X_m & 0 \\ 0 & -X_m \end{pmatrix},$$
$$\mathbf{a}^p = 0, \quad \mathbf{b}^p = 0 \tag{11}$$

and folded along $\theta = 45^\circ$.

We start with the case of $X_m = X$, folded into a cylinder, with $\theta = 45^\circ$ where we find two types of solutions for each mode index n, corresponding to two distinct dispersion branches. The dispersion equations are

$$8nXk_z a I_n K_n - \tau a[(X \mp 2)^2 I_n{}' K_n - (X \pm 2)^2 I_n K_n{}'] = 0, \tag{12}$$

where the upper and lower signs correspond to the two distinct solution families. The dispersion curves are shown in Fig. 3(b) for $X = -4$, and the modal fields satisfy

$$E_z^{i,o}(r = a) = \pm j\eta_0 H_z^{i,o}(r = a), \tag{13}$$

regardless of X. When substituting the dispersion solutions back into the governing equations [Eqs. (A8) in Appendix A] to obtain the mode profile, the difference between the two

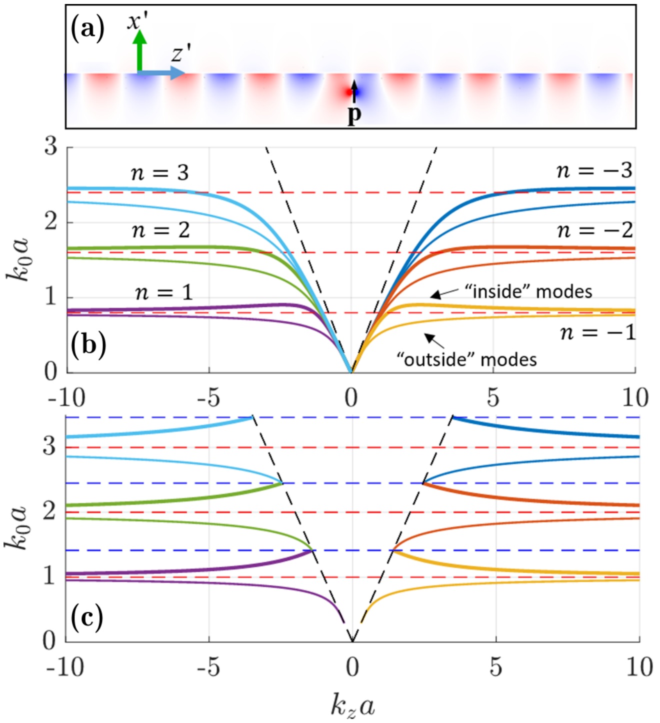

FIG. 3. (a) Excitation of surface waves over a *planar* surface with $Y_{y'y'} = -j0.3/\eta_0$, $Y_{z'z'} = j16.133/\eta_0$ and $\Omega = 0.2$, corresponding to Eq. (10). The modal fields are concentrated at the bottom surface. (b) Surface wave dispersion curves for a cylinder with electric surface admittance and magnetic surface impedance satisfying $\underline{\underline{\mathbf{Z}}}^p_{ms} = \eta_0^2\underline{\underline{\mathbf{Y}}}^p_s$, corresponding to $X = X_m = -4$ in Eq. (11). Dashed black lines are the light lines and $k_0 = \omega/c$. Thin lines correspond to the family of modes concentrated mostly on the outer part of the cylinder, and thick lines correspond to the family of modes concentrated mostly on the inner part of the cylinder, as described by Eqs. (12) and (14). (c) Same as (b) but with $X = X_m = -2$.

modal solutions becomes apparent. The field amplitudes on the tube surface [both electric and magnetic, according to Eq. (13)] satisfy

$$\frac{|E_z^i|}{|E_z^o|} = \frac{|H_z^i|}{|H_z^o|} = \frac{(X \pm 2)}{(X \mp 2)}, \tag{14}$$

yielding that the first set of modes is concentrated mostly inside the cylinder (denoted by thick lines), while the second is on the outer region (denoted by thin lines), corresponding to the labels in Fig. 3(b). This figure also shows that, by tuning the operation frequency to be slightly above or below $f_{r,n}$, we can control which field distribution is dominant.

When $X = \pm 2$, we maximize the contrast between inside and outside fields, yielding slow-wave modes concentrated purely in the interior or exterior part of the cylinder. In this extreme scenario, the modes are not only spatially separated, but also totally spectrally separated—they are guided in completely different frequency bands, as shown in Fig. 3(c). New cutoff frequencies at $k_{0,c}a = \sqrt{n(n+1)}$ are induced in this regime (dashed blue lines in the figure). In this scenario, Eq. (13) ensures that $\mathrm{sgn}(\mathfrak{S}^{i,o}_\infty) = \mp 1$, coupling the helicity to the geometrical domain where the fields are concentrated.

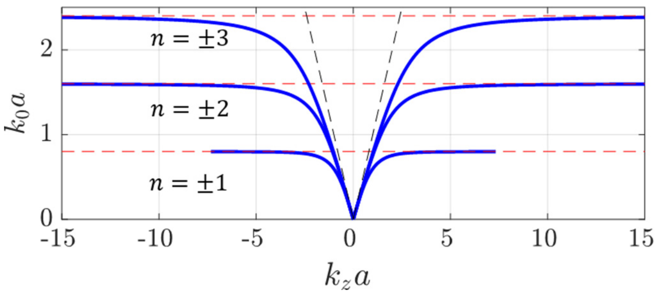

FIG. 4. Dispersion curves for a folded metasurface, corresponding to $X_m = -4/X$ in Eq. (11). The surface parameters are $X = 4$, $X_m = -1$, and the folding angle is $\theta = \pi/4$. Black dashed lines are the light lines, and $k_0 = \omega/c$.

Another interesting class corresponds to the same relation as in Eq. (11), this time with $X_m = -4/X$. As before we perform the folding along the $\theta = 45^\circ$ line. The dispersion equation obtained in this case is completely symmetric for propagation to the left and right directions,

$$|nk_z| = \frac{(k_0a)(\tau a)}{4|X|}\sqrt{\left(4\frac{K_n'}{K_n} - \frac{I_n'}{I_n}X^2\right)\left(\frac{K_n'}{K_n}X^2 - 4\frac{I_n'}{I_n}\right)}, \tag{15}$$

and the curves obtained are shown in Fig. 4 for $X = -4$. The asymmetry in this case is revealed when closely examining the helicity of the propagating modes, satisfying $\mathrm{sgn}(\mathfrak{S}^{i,o}_\infty) = \mathrm{sgn}(nk_z)$ and exhibiting strong helicity-momentum-OAM coupling.

Additionally, it is worth mentioning the case of $X_m = -X$. Here, no such pronounced asymmetry is present, however it allows tailoring of the TE/TM ratio of the propagating waves. If we denote this ratio ζ (the same notation is also used in Appendix B) we obtain

$$|\zeta| = \frac{|E_z|}{|\eta_0 H_z|} = \left|\frac{X}{2}\right| \tag{16}$$

with a dispersion curve very similar to the previous case, presented in Fig. 4.

V. CONCLUSIONS

In this paper, we have explored surface wave propagation over metasurface tubes. We have shown that folded hyperbolic metasurfaces can form an interesting platform for nanophotonics and valleytronics applications. They yield highly asymmetric propagation properties in terms of angular momentum, enabling largely unusual responses when properly tuning their impedance parameters. Around the resonance frequencies, the structures obtained may strongly interact with OAM/spin carrying waves such as the vortex Laguerre-Gauss beams [21] (with many more examples in [22]) or spin-specific excitons [36,48,49] which utilize the valley degree of freedom in transition metal dichalcogenides. When incorporating magnetic response of a similar nature, these tubes also give rise to tunable asymmetry such as high field contrast between the inner and outer domains in addition to the asymmetric propagation. For all of the cases studied, strong OAM-momentum coupling was demonstrated which can be viewed as an extension of the spin-momentum coupling present in topological edge states.

For each studied case, it was shown that the sign of the optical helicity for the propagating waves is controlled and coupled to various parameters—surface impedance, field propagation domain, OAM, and wave number.

APPENDIX A: DERIVATION OF THE EM FIELDS AND DISPERSION EQUATION

To obtain the dispersion equation, we start by expressing the tangent fields using the coefficients A^i, A^o, B^i, B^o defined in Eq. (3), arranged in a vector $\mathbf{C}^{i,o} = (A^{i,o}, B^{i,o})^T$,

$$\mathbf{E}^{i,o}_{\text{tan}} = e^{-jn\varphi}e^{-jk_z z}\underline{\underline{\mathbf{M}}}_{E,(i,o)}\mathbf{C}^{i,o},$$
$$\mathbf{H}^{i,o}_{\text{tan}} = e^{-jn\varphi}e^{-jk_z z}\underline{\underline{\mathbf{M}}}_{H,(i,o)}\mathbf{C}^{i,o}, \tag{A1}$$

with

$$\mathbf{C}^i = \begin{bmatrix} A^i_n \\ B^i_n \end{bmatrix} \quad \mathbf{C}^o = \begin{bmatrix} A^o_n \\ B^o_n \end{bmatrix}, \tag{A2}$$

and the matrices $\underline{\underline{\mathbf{M}}}_E, \underline{\underline{\mathbf{M}}}_H$ are defined as [24,39]

$$\underline{\underline{\mathbf{M}}}_{E,i} = \begin{bmatrix} \frac{nk_z}{\tau^2}I_n(\tau a) & -\frac{jk_0 a}{\tau}I_n{}'(\tau a) \\ I_n(\tau a) & 0 \end{bmatrix}, \tag{A3}$$

$$\underline{\underline{\mathbf{M}}}_{E,o} = \begin{bmatrix} \frac{nk_z}{\tau^2}K_n(\tau a) & -\frac{jk_0 a}{\tau}K_n{}'(\tau a) \\ K_n(\tau a) & 0 \end{bmatrix}, \tag{A4}$$

$$\underline{\underline{\mathbf{M}}}_{H,i} = \begin{bmatrix} \frac{jk_0 a}{\tau}I_n{}'(\tau a) & \frac{nk_z}{\tau^2}I_n(\tau a) \\ 0 & I_n(\tau a) \end{bmatrix}, \tag{A5}$$

$$\underline{\underline{\mathbf{M}}}_{H,o} = \begin{bmatrix} \frac{jk_0 a}{\tau}K_n{}'(\tau a) & \frac{nk_z}{\tau^2}K_n(\tau a) \\ 0 & K_n(\tau a) \end{bmatrix}. \tag{A6}$$

To easily substitute these relations into the boundary conditions, we represent the $\hat{\mathbf{r}}\times$ operation that would be needed in Eqs. (1) and (2) using a 2×2 matrix $\hat{\mathbf{r}} \times \mathbf{V}_{\text{tan}} = \underline{\underline{\mathbf{N}}}_r \mathbf{V}_{\text{tan}}$, where $\mathbf{V}_{\text{tan}}$ is any tangential column vector of the form $\mathbf{V}_{\text{tan}} = [V_\varphi, V_z]^T$, and $\underline{\underline{\mathbf{N}}}_r = \left(\begin{smallmatrix} 0 & -1 \\ 1 & 0 \end{smallmatrix}\right)$.

We also define the unitless response matrices $\underline{\underline{\mathbf{X}}}_s, \underline{\underline{\mathbf{X}}}_{ms}$,

$$\underline{\underline{\mathbf{Y}}}_s = j\underline{\underline{\mathbf{X}}}_s/\eta_0, \quad \underline{\underline{\mathbf{Z}}}_{ms} = j\underline{\underline{\mathbf{X}}}_{ms}\eta_0. \tag{A7}$$

To express the boundary conditions over the rotated and folded cylindrical sheath, we rotate each of the fields by the angle $-\theta$ with respect to $\hat{\mathbf{z}}$, and then rotate the result back by θ to the lab frame. This results in rotated response matrices of the form $\underline{\underline{\mathbf{m}}}_s = \underline{\underline{\mathbf{R}}}^\theta \underline{\underline{\mathbf{m}}}^p_s \underline{\underline{\mathbf{R}}}^{-\theta}$, where $\underline{\underline{\mathbf{m}}}_s$ is any of the tensors defined in the constitutive relations in Eqs. (1) and (2), $\underline{\underline{\mathbf{m}}}^p_s$ are the response matrices of the principal planar surface (in axes z', y' as defined in the main text), and $\underline{\underline{\mathbf{R}}}^\theta$ is the two-dimensional rotation matrix by angle θ. By substituting these into the boundary conditions in Eqs. (1) and (2) we obtain

$$\underline{\underline{\mathbf{M}}}\mathbf{C} = \begin{bmatrix} \frac{1}{2}\underline{\underline{\mathbf{X}}}_s\underline{\underline{\mathbf{M}}}_{E,i} + \left(\frac{1}{2}\underline{\underline{\mathbf{a}}} + \underline{\underline{\mathbf{N}}}_r\right)\underline{\underline{\mathbf{M}}}_{H,i} & \frac{1}{2}\underline{\underline{\mathbf{X}}}_s\underline{\underline{\mathbf{M}}}_{E,o} + \left(\frac{1}{2}\underline{\underline{\mathbf{a}}} - \underline{\underline{\mathbf{N}}}_r\right)\underline{\underline{\mathbf{M}}}_{H,o} \\ \left(\frac{1}{2}\underline{\underline{\mathbf{b}}} - \underline{\underline{\mathbf{N}}}_r\right)\underline{\underline{\mathbf{M}}}_{E,i} + \frac{1}{2}\underline{\underline{\mathbf{X}}}_{ms}\underline{\underline{\mathbf{M}}}_{H,i} & \left(\frac{1}{2}\underline{\underline{\mathbf{b}}} + \underline{\underline{\mathbf{N}}}_r\right)\underline{\underline{\mathbf{M}}}_{E,o} + \frac{1}{2}\underline{\underline{\mathbf{X}}}_{ms}\underline{\underline{\mathbf{M}}}_{H,o} \end{bmatrix}\begin{bmatrix} \mathbf{C}^i \\ \mathbf{C}^o \end{bmatrix} = 0. \tag{A8}$$

For a nontrivial solution to exist, we need $\text{Det}\{\mathbf{M}\} = 0$, providing the dispersion equation for propagating waves.

APPENDIX B: CALCULATION OF THE HELICITY

We use the helicity density $\mathfrak{S}$ definition from [35,46], which reads for our case

$$\mathfrak{S} = \frac{1}{2\omega}\text{Im}\{\mathbf{H}^* \cdot \mathbf{E}\}. \tag{B1}$$

In addition, for all cases examined in the main text, the relation between the TE and TM components can be characterized by

$$\eta_0 B^{i,o}_n = j\zeta_{i,o}A^{i,o}_n \tag{B2}$$

with $\zeta \in \mathbb{R}$ being a unitless proportionality constant, and $B^{i,o}_n, A^{i,o}_n$ defined in Eq. (3). This lets us write the helicity density of the guided fields as

$$\mathfrak{S}^i = -\frac{\left|A^i_n\right|^2}{2\omega\bar{\tau}^4}\left[\zeta_i I^2_n(\bar{\tau})\left[\bar{\tau}^4 + n^2\left(\bar{k}^2_z + \bar{a}^2\right)\right] + \zeta_i I'^2_n(\bar{\tau})\bar{\tau}^2\left(\bar{k}^2_z + \bar{a}^2\right) + 2I_n I'_n n\bar{k}^2_z\bar{\tau}\bar{a}\left(1 + \zeta^2_i\right)\right],$$
$$\mathfrak{S}^o = -\frac{\left|A^o_n\right|^2}{2\omega\bar{\tau}^4}\left[\zeta_i K^2_n(\bar{\tau})\left[\bar{\tau}^4 + n^2\left(\bar{k}^2_z + \bar{a}^2\right)\right] + \zeta_i K'^2_n(\bar{\tau})\bar{\tau}^2\left(\bar{k}^2_z + \bar{a}^2\right) + 2K_n K'_n n\bar{k}^2_z\bar{\tau}\bar{a}\left(1 + \zeta^2_i\right)\right] \tag{B3}$$

with $\bar{k}_z = k_z a$, $\bar{\tau} = \tau a$, $\bar{a} = k_0 a$. In our work we study the highly confined waves, with large wave numbers, letting us simplify this expression significantly,

$$\mathfrak{S}^i_\infty = -\frac{\left|A^i_n\right|^2\zeta_i}{2\omega}\left[I^2_n(\bar{\tau}) + I'^2_n(\bar{\tau})\right], \quad \mathfrak{S}^o_\infty = -\frac{\left|A^i_n\right|^2\zeta_i}{2\omega}\left[K^2_n(\bar{\tau}) + K'^2_n(\bar{\tau})\right], \tag{B4}$$

based on large-argument approximations of the modified Bessel functions [50], where we used the symbol $\mathfrak{S}_\infty = \mathfrak{S}(\beta \gg k_0)$. This result is valid as long as ζ is not strongly dependent on $\bar{\beta}$, which is indeed the case in all of the systems examined. It is important to note that for any value of $\bar{\tau}$ the expressions in the square brackets are positive, therefore, the sign of the helicity density is determined solely by the sign of ζ, and satisfies

$$\mathrm{sgn}\big(\mathfrak{S}^{i,o}_{\infty}\big) = -\mathrm{sgn}(\zeta^{i,o}). \tag{B5}$$

[1] S. B. Glybovski, S. A. Tretyakov, P. A. Belov, Y. S. Kivshar, and C. R. Simovski, Phys. Rep. **634**, 1 (2016).

[2] S. Tretyakov, *Analytical Modeling in Applied Electromagnetics* (Artech House, Boston, London, 2003).

[3] H. J. Bilow, IEEE Trans. Antennas Propag. **51**, 2788 (2003).

[4] C. L. Holloway, D. C. Love, E. F. Kuester, J. A. Gordon, and D. A. Hill, IEEE Trans. Antennas Propag. **60**, 5173 (2012).

[5] C. L. Holloway, E. F. Kuester, J. A. Gordon, J. O'Hara, J. Booth, and D. R. Smith, IEEE Antennas Propag. Mag. **54**, 10 (2012).

[6] I. V Lindell, A. H. Sihvola, S. A. Tretyakov, and A. J. Viitanen, *Electromagnetic Waves in Chiral and Bi-Isotropic Media* (Artech House, Boston, London, 1994).

[7] C. Pfeiffer and A. Grbic, Phys. Rev. Lett. **110**, 197401 (2013).

[8] K. Achouri, M. A. Salem, and C. Caloz, IEEE Trans. Antennas Propag. **63**, 2977 (2015).

[9] A. Epstein and G. V. Eleftheriades, IEEE Trans. Antennas Propag. **64**, 3880 (2016).

[10] J. S. Gomez-Diaz, M. Tymchenko, and A. Alù, Phys. Rev. Lett. **114**, 233901 (2015).

[11] J. S. Gomez-Diaz, M. Tymchenko, and A. Alù, Opt. Mater. Express **5**, 2313 (2015).

[12] J. S. Gomez-Diaz and A. Alù, ACS Photon. **3**, 2211 (2016).

[13] O. Y. Yermakov, A. I. Ovcharenko, M. Song, A. A. Bogdanov, I. V. Iorsh, and Y. S. Kivshar, Phys. Rev. B **91**, 235423 (2015).

[14] D. R. Smith and D. Schurig, Phys. Rev. Lett. **90**, 077405 (2003).

[15] A. Sommerfeld, Ann. Phys. **303**, 233 (1899).

[16] G. Goubau, J. Appl. Phys. **21**, 1119 (1950).

[17] I. A. Kotelnikov and G. V. Stupakov, Phys. Lett. A **379**, 1187 (2015).

[18] H. Barlow, IRE Trans. Antennas Propag. **7**, 147 (1959).

[19] R. S. Elliott, J. Appl. Phys. **26**, 368 (1955).

[20] J. A. Stratton, *Electromagnetic Theory* (McGraw-Hill, New York, 1941).

[21] L. Allen, M. W. Beijersbergen, R. J. C. Spreeuw, and J. P. Woerdman, Phys. Rev. A **45**, 8185 (1992).

[22] M. J. Padgett, Opt. Express **25**, 11265 (2017).

[23] J. R. Pierce and P. K. Tien, Proc. IRE **42**, 1389 (1954).

[24] D. A. Watkins, *Topics in Electromagnetic Theory* (John Wiley & Sons, New York, 1958).

[25] G. Y. Slepyan, S. A. Maksimenko, A. Lakhtakia, O. M. Yevtushenko, and A. V. Gusakov, Phys. Rev. B **57**, 9485 (1998).

[26] G. Ya. Slepyan, S. A. Maksimenko, A. Lakhtakia, O. Yevtushenko, and A. V. Gusakov, Phys. Rev. B **60**, 17136 (1999).

[27] P. Y. Chen and A. Alù, Phys. Rev. B **84**, 205110 (2011).

[28] T. Bian, X. Gao, S. Yu, L. Jiang, J. Lu, and P. T. Leung, Optik (Stuttg). **136**, 215 (2017).

[29] T. Christensen, A. P. Jauho, M. Wubs, and N. A. Mortensen, Phys. Rev. B **91**, 125414 (2015).

[30] A. Sihvola, D. C. Tzarouchis, P. Ylä-Oijala, H. Wallén, and B. Kong, Phys. Rev. B **98**, 235417 (2018).

[31] R. Ruppin, J. Phys.: Condens. Matter **16**, 5991 (2004).

[32] V. Kuzmiak and A. A. Maradudin, Phys. Rev. B **66**, 045116 (2002).

[33] M. Safari, A. Abdolali, H. Kazemi, M. Albooyeh, M. Veysi, and F. Capolino, in *2017 IEEE International Symposium on Antennas and Propagation & USNC/URSI National Radio Science Meeting* (IEEE, Piscataway, NJ, 2017), pp. 1499–1500.

[34] L. Wang, S. Li, B. Zhang, Y. Qin, Z. Tian, Y. Fang, Y. Li, Z. Liu, and Y. Mei, ACS Appl. Mater. Interfaces **10**, 7704 (2018).

[35] F. Alpeggiani, K. Y. Bliokh, F. Nori, and L. Kuipers, Phys. Rev. Lett. **120**, 243605 (2018).

[36] K. F. Mak, K. He, J. Shan, and T. F. Heinz, Nat. Nanotechnol. **7**, 494 (2012).

[37] C. Pfeiffer and A. Grbic, Phys. Rev. Appl. **2**, 044011 (2014).

[38] J. A. Kong, Proc. IEEE **60**, 1036 (1972).

[39] D. M. Pozar, *Microwave Engineering*, 4th ed. (John Wiley, Hoboken, NJ, 2012).

[40] L. Sun, C. Y. Wang, A. Krasnok, J. Choi, J. Shi, J. S. Gomez-Diaz, A. Zepeda, S. Gwo, C. K. Shih, A. Alù, and X. Li, Nat. Photon. **13**, 180 (2019).

[41] A. B. Khanikaev, S. H. Mousavi, W.-K. Tse, M. Kargarian, A. H. MacDonald, and G. Shvets, Nat. Mater. **12**, 233 (2013).

[42] P. V. Kapitanova, P. Ginzburg, F. J. Rodríguez-Fortuño, D. S. Filonov, P. M. Voroshilov, P. A. Belov, A. N. Poddubny, Y. S. Kivshar, G. A. Wurtz, and A. V. Zayats, Nat. Commun. **5**, 3226 (2014).

[43] R. E. Collin, *Field Theory of Guided Waves* (Oxford University Press, Oxford, 1995).

[44] COMSOL Multiphysics® v. 5.4. www.comsol.com, COMSOL AB, Stockholm, Sweden.

[45] This was calculated by sampling the electric field on a circle around the cylinder, halfway between the sources and the right edge. the result was then fourier transformed to obtain the modal content.

[46] K. Y. Bliokh, Y. S. Kivshar, and F. Nori, Phys. Rev. Lett. **113**, 033601 (2014).

[47] J. A. Kong, *Electromagnetic Wave Theory* (EMW, Cambridge, MA, 2005).

[48] A. Krasnok, S. Lepeshov, and A. Alú, Opt. Express **26**, 15972 (2018).

[49] J. R. Schaibley, H. Yu, G. Clark, P. Rivera, J. S. Ross, K. L. Seyler, W. Yao, and X. Xu, Nat. Rev. Mater. **1**, 16055 (2016).

[50] F. W. J. Olver, D. W. Lozier, R. F. Boisvert, and C. W. Clark, *NIST Handbook of Mathematical Functions* (Cambridge University Press, Cambridge, 2010).